Tribology International 42 (2009) 699–705

Contents lists available at ScienceDirect

Tribology International

journal homepage: www.elsevier.com/locate/triboint

Increasing nanohardness and reducing friction of nitride steel by laser surface texturing ☆

E. Gualtieri [a,b,*], A. Borghi [a], L. Calabri [a], N. Pugno [c], S. Valeri [a,b]

[a] CNR-INFM-National Research Centre on NanoStructures and BioSystems at Surfaces (S^3), via Campi 213/a, 41100 Modena, Italy
[b] Department of Physics, Università degli Studi di Modena e Reggio Emilia, via Campi 213/a, 41100 Modena, Italy
[c] Department of Structural Engineering, Politecnico di Torino, Corso Duca degli Abruzzi 24, 10129 Torino, Italy

ARTICLE INFO

Article history:
Received 30 August 2007
Received in revised form
25 August 2008
Accepted 23 September 2008
Available online 10 October 2008

Keywords:
Surface texture
Friction measurement
Nanoindentation
Atomic force microscope

ABSTRACT

Laser surface texturing is often employed to improve tribological performances of mating surfaces. The principal aim of the present work is to study local modifications induced by laser beam during the texturing process (microdimpling), on the mechanical properties of a 30NiCrMo12 nitride steel.

A brief tribological characterization was initially made in order to verify the improvement of tribological behaviour ensured by microdimpling. Friction measurements were carried out in lubricated flat-on-flat and round-on-flat configurations.

A sub-surface characterization was performed by focused ion beam cross-section and imaging. Modified material layers were discovered in correspondence of laser-affected zones around dimples, where grain dimensions were observed to be reduced. To quantify this phenomenon, a new theoretical energetic model was developed.

Hardness measurements were performed by atomic force microscope nanoindentation. This approach allowed to observe an hardening effect moving from bulk material to dimple edges. Therefore, the theoretical model was integrated with the Hall–Petch's law in order to quantify the observed hardening behaviour.

1. Introduction

Steels are representative structural materials for almost all kinds of mechanical applications because of their high strength and toughness, good machinability and low cost. Surface hardness and composition play a dominant role against wear under sliding conditions. The efficiency, reliability, and durability of mating mechanical components depend on friction occurring at the interface during the sliding. In addition, the increase in load capacity and power density of engine elements leads to higher intensities of surface interactions. Both the need to reduce friction and the desire to increase power require effective lubrication strategy for sliding surfaces [1].

It has been demonstrated that the presence of artificially created microfeatures can significantly affect tribological behaviour of lubricated surfaces: specific textures may trap wear particles and reduce ploughing and friction of surfaces, thus increasing the lifetime of the sliding contacts [2–4]. Indeed, when irregularities cover the surface with a sufficient density, they can improve the oil wetting of the surface and thereby facilitate the lubricating film formation promoting its retention between mating surfaces. At higher sliding speed, and with a sufficient supply of oil, individual surface cavities, or grooves, may act as hydrodynamic pressure pockets, reducing friction [5–7]. Various manufacturing methods are utilized to produce textures on contact surfaces (mechanical and lithographical methods, coatings and energy beam techniques [8]). Among these, laser surface texturing (LST) offers promising features: extremely fast processing time, clean to the environment and excellent control of the aspect-ratio of the micro-holes [9–11]. By controlling the orientation of the laser beam, and tuning the characteristics of the spot it is possible to easily texture a wide range of material, with no need of vacuum. This technique allows covering samples by regular arrays of ablated dimples, with different size and shape (typically spherical or cylindrical).

Several classes of tribological experiments were developed in order to investigate the benefits of LST in terms of transition between different lubrication regimes, reduction of friction coefficients and reduction of wear rates, mainly on steel surfaces [2–4,7–12]. However, the present work intends to face also another specific aspect of this topic. As a matter of fact, there is

☆ Presented at the 34th Leeds-Lyon Symposium on Tribology, Lyon, 4th to 7th September 2007.

* Corresponding author at: Department of Physics, Università degli Studi di Modena e Reggio Emilia, via Campi 213/a, 41100 Modena, Italy.
Tel.: +39 059 2055741; fax: +39 059 2055235.
E-mail address: egualtieri@unimore.it (E. Gualtieri).

0301-679X/$ - see front matter © 2008 Elsevier Ltd. All rights reserved.
doi:10.1016/j.triboint.2008.09.008

a lack of information about the possible "additional effects" of the LST process as a consequence of the interaction between laser beam and material structure. Ablation of surface is accompanied to local annealing, which could activate phase transitions in correspondence of the laser-affected zone: laser beam interaction plays a key role in heat propagation, which could result in the formation of modified material layers. Laser heating causes several phenomena, in particular on steel surfaces: variations in dislocations and residual stresses distributions, formation of different carbide types, size and shape modification of austenitic grains and hardening effects [13–15].

The core of the present work is focused on the investigation of laser–steel interaction in terms of morphological and structural sub-surface modifications on laser textured nitride steels. 30NiCrMo12 nitride steel has been studied. This material (bulk composition: 3.00%Ni, 0.80Cr, 0.45Mo, 0.3C, all in wt%) is employed for automotive application due to its surface strength guaranteed by hot nitriding treatment. Focused ion beam (FIB) was utilized to explore local properties: thanks to its versatility and ability to remove and observe trenches of surface without introducing relevant additional damage, this approach is adopted to characterize sub-surface micro-cracking, defects distributions and grain structure of material surfaces [16–18]. Sub-surface micro-hardness measurements were also performed by indenting a cross-section of the specimen material by using atomic force microscope (AFM) working in nanoindentation mode. Thanks to its ability of simultaneous high resolution indenting and imaging, this powerful tool allows the investigation of the hardness distribution in sub-micrometric areas [19,20].

2. Experimental details

Samples were prepared as discs 26 mm in diameter and 8 mm thick. The discs were first lapped to obtain a surface roughness (Ra) of 0.05 μm, then textured by LST. Table 1 contains a description of the principal parameters of the laser apparatus adopted for the treatment. Textured nitride steel discs show regular arrays of circular dimples with a diameter of 100 μm, a depth of 50 μm and a surface density of 40% (Fig. 1).

Friction tests were performed using a UMT-2 tribometer (provided by CETR®). During the tests, a constant normal load was applied on the samples, which slid at different linear speeds ranging between 0.06 and 40 cm s^{-1} (corresponding to an angular velocity which ranges between 0.3 and 200 rpm). Friction coefficient evolution was recorded in a "full lubrication" configuration, with the mating counterparts full immerged in a bath of a commercial oil (Vanguard® ST-46). Both untextured and textured steels were tested for comparison.

Morphological characterization was performed using a dual beam system (FEI® StrataTM DB235), combining a high-resolution FIB column equipped with a Ga liquid metal ion source (LMIS) and a SEM column equipped with a Schottky field emission gun (SFEG) electron source. Perpendicular "micro-cross-sections" of steel surfaces (textured and untextured) were obtained using FIB ($E_{beam} = 30$ KeV) as micro-machining miller, setting 5 nA as ion beam current for first rough trench, and 1 nA for final polishing. Sub-surface discovered wall is one side of the perpendicular trench, milled by progressive steps (Fig. 2). In order to prevent the topmost material from mechanical intermixing upon contact with energetic ions [16], the surface sample was protected by a thin platinum layer (1 μm thickness). A Pt-shield had been grown starting from a gas precursor, and using a 10 pA ion beam current that assisted local deposition. Furthermore, by tilting the sample holder, images of discovered walls were obtained collecting secondary electrons generated by FIB as primary beam at low current (50 pA), in order to take advantage of ion-channelling contrast, which is very useful for grain size analysis [21].

Afterwards textured samples were perpendicularly cut with a saw, in order to obtain "macro-cross-sections" and then polished with SiC papers and diamond slurry (up to 0.05 μm Ra). Micro-indentation grids were finally performed on these samples on selected areas around dimples (Fig. 3), by using a *Digital Instruments EnviroScope Atomic Force Microscope* (provided by *Veeco*®) working in nanoindentation mode, in order to indent the

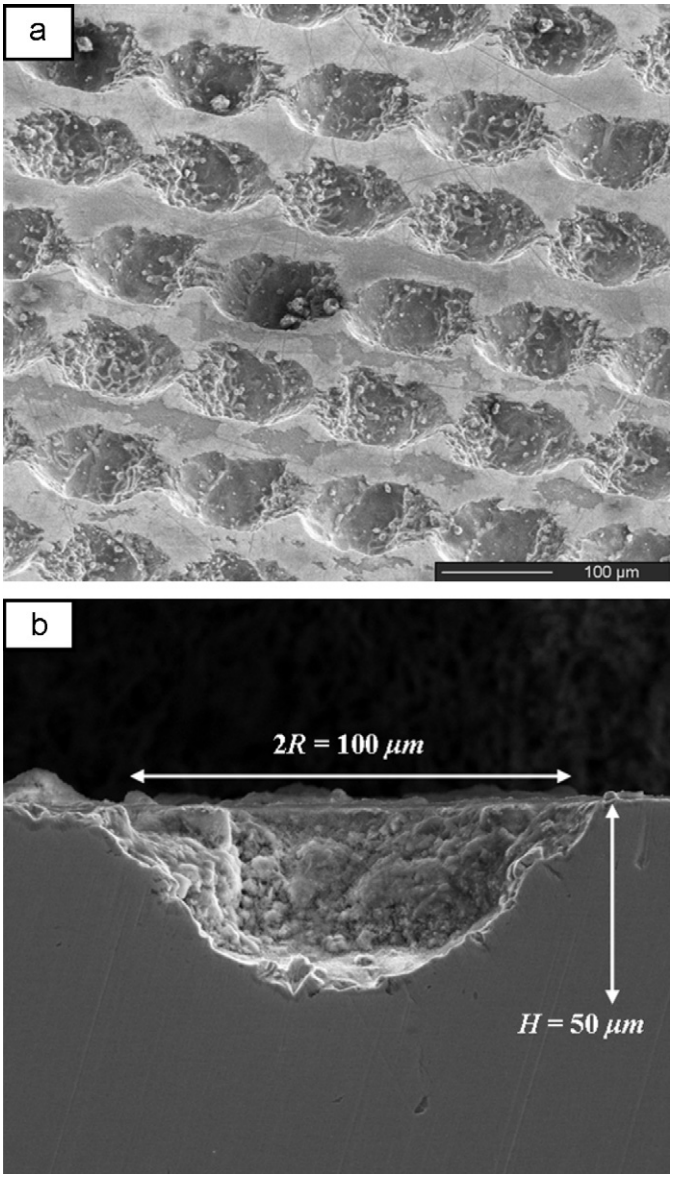

Fig. 1. SEM images of 30NiCrMo12 nitride steel textured surface: (a) 45° tilted top view and (b) perpendicular cross-section of a singular sectioned dimple: the shape could be approximated as hemi-spherical.

Table 1
Details of the laser apparatus utilized to produce LST microdimples

Laser type	"Spectron" Nd:YAG
Laser beam wavelength	1.06 μm
Pulses duration	30 ns
Laser beam energy per pulsation	4 mJ

Laser scanning was carried out by CNC *X–Y* table under special program providing definite pore position.

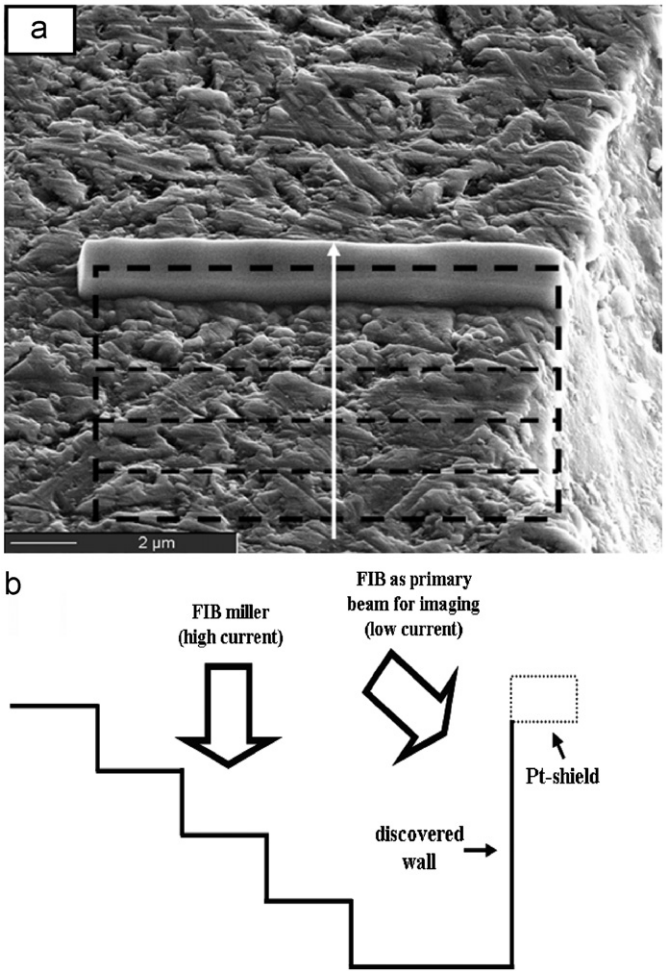

Fig. 2. Simplified sketch which summarizes the experimental procedures followed in order to carry out a morphological sub-surface characterization. SEM image (a) shows the thin Pt-shield grown in-situ, beside a dimple edge, by a FIB-assisted deposition. Dotted lines represent the projection of the trench, successfully milled by FIB setting high ion current mode. Thus, a "micro-cross-section" was gained by progressive rastering steps: white arrow indicates the relative depth profile (b). Sub-surface discovered wall was imaged using FIB as primary probe (low current mode), by tilting the sample holder.

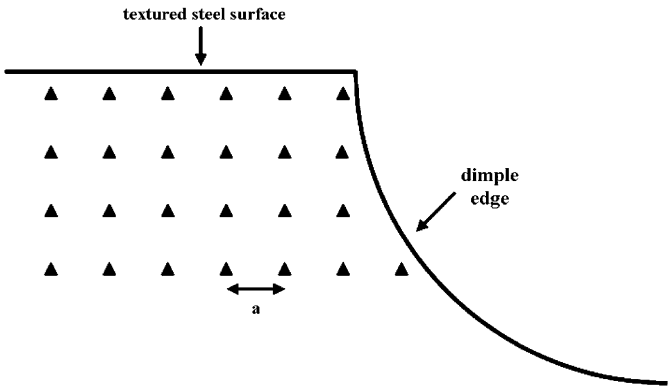

Fig. 3. Simplified sketch which summarizes the experimental procedures followed in order to carry out a mechanical sub-surface characterization of "macro-cross-sectioned" textured steel samples. A micro-indentation grid was realized, and successfully imaged by AFM on selected areas around dimple edges. Spacing between two adjacent indentations ($a \approx 1\,\mu m$) is maintained constant, but could slightly change in proximity of the border, in order to faithfully follow the shape of the dimple edge.

sample and image it right after the indentation. All the indentations were performed by a Berkovich diamond tip mounted on a sapphire cantilever (the whole probe had been assembled and provided by *Micro Star Technologies*®) under the same conditions; in particular the load applied on the sample was 1.5 V in terms of photodetector voltage. Thus, considering the cantilever stiffness ($5085\,N\,m^{-1}$) and the deflection sensitivity ($130\,V\,nm^{-1}$), a maximum indentation load of about 992 μN was estimated. Further details on this setup are reported in [20]. Finally, the indented area was imaged using a standard AFM tapping probe (*MPP*-11100-*Tap*300 *Metrology Probes* by *Veeco*®) in order to measure the projected contact area in a direct way and thus evaluate the hardness just dividing the maximum load by this area. This approach allows to solve the pile-up problem, which affects the results in the Oliver–Pharr method [22–24]. The O–P approach guarantees hardness measurement without imaging the indentation impression, since it establishes a relationship between the projected area of the indentation impression, the maximum depth of indentation (h_{max}) and the initial unloading stiffness (S), where h_{max} and S are both measurable from the load–displacement curve. However, the Oliver–Pharr method quite overestimates the hardness values when the pile-up effect is not negligible, such in this case. With AFM nanoindentation, since it is possible to measure directly the contact area, we are able to take into account the actual presence of pile-up [20].

3. Results and discussion

3.1. Friction measurements

The experimental analysis was carried out comparing the performances of textured and untextured surfaces under the same tribological conditions, repeating each individual test in order to verify the reproducibility of the results.

Average values of friction coefficients (considering standard deviations as error bars) were summarized in the form of a Stribeck curve (Fig. 4a), obtained showing the friction coefficient as a function of Stribeck parameter, calculated as the ratio between v (linear speed) and W (nominal contact pressure) and assuming the lubricant viscosity (η) as constant. In the case reported in Fig. 4a the pin-on-disk mode was exploited. Conformal contact was obtained by using a smooth stainless steel pin as static counterpart with a round contact area of 5.5 mm in diameter. Thus, the nominal flat-on-flat contact pressure was roughly 0.2 MPa. Different ranges of mating speeds were explored applying a constant normal load (4.5 N), thus ranging the Stribeck parameter roughly between 0.3 and $200\,cm\,s^{-1}\,MPa^{-1}$.

During the whole experimental analysis, both systems (textured and untextured) operated in hydrodynamic lubrication regime because of the massive presence of lubricant, even when the tribological conditions became more severe (low speeds and Stribeck parameter lower than $10\,cm\,s^{-1}\,MPa^{-1}$). The trend of the curves reported in Fig. 4a (roughly constant) shows no significant transition towards boundary or mixed lubrication regimes. Nevertheless, the textured surface exhibits considerable lower friction coefficient than untextured surface. The reason is ascribable to the higher hydrodynamic lift ensured by the dimples regularly distributed on the contact area, thus capable to behave as integrated pressure pockets.

Subsequently an endurance test was performed on both textured and untextured discs. In this case the tribometer was configured in ball-on-disk mode: static counterpart was a stainless steel ball (diameter: 4 mm), and the test was carried out applying a normal load of 4 N (the nominal contact pressure reaches about 1 GPa estimating by Hertzian model). Mating

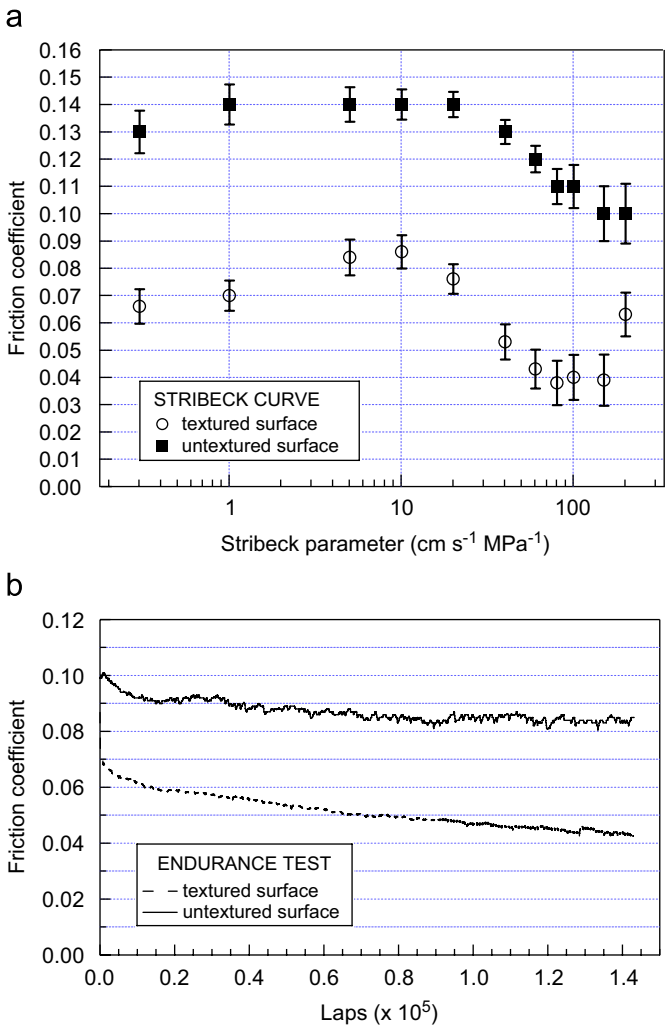

Fig. 4. (a) Stribeck curves: friction coefficients against Stribeck parameters calculated as the ratio between mating speeds (ranging from 0.06 to 40 cm s^{-1}) and nominal contact pressures (maintained constant: roughly 0.2 MPa). (b) Endurance test: comparison of the evolution of the friction coefficients (plotted as a function of the number of laps) relative to untextured case (continuous line) and textured case (dotted line).

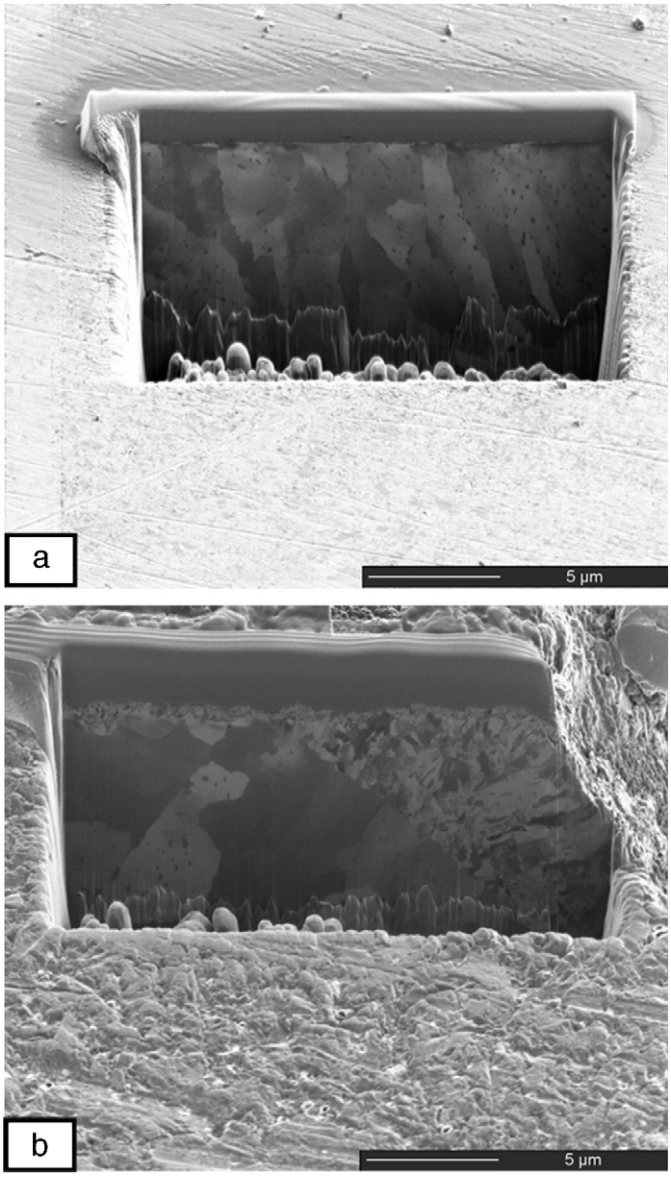

Fig. 5. FIB images obtained by tilting samples after sub-surface FIB micro-trenches milled on (a) untextured and (b) textured 30NiCrMo12 nitride steel. Dimple edge is visible on the top corner of (b).

counterparts slid for 4 h at a sliding speed of 40 cm s^{-1}. Friction coefficient evolution was monitored during the test and the results are reported in Fig. 4b as a function of number of laps. The textured surface maintained lower friction coefficient values for the whole endurance test with respect to the untextured surface. Further details about this experimental analysis are reported in [12].

3.2. Sub-surface morphological characterization

Fig. 5a shows a FIB image obtained in correspondence will a FIB milled "micro-cross-section" on untextured steel. Discovered wall extends 20 μm in width and 7 μm in depth. Ion-channelling contrast allows appreciation of a sub-surface polygonal structure: clear defined boundaries delimit large domains (areas: up to 10 μm^2) which include isolated features ("dark" signals) of round or polygonal shape (sizes: 200–300 nm). These features could be associated to steel porosity or C/N-compounds. The possible presence of carbides and nitrides is justified by the not negligible presence of Cr an C dispersed in steel, or ascribable to nitriding process.

FIB milled "micro-cross-sections" were also obtained beside dimples on textured steel. Also in this case, discovered walls are 7 μm deep and 20 μm wide from the edge of dimples. Sub-surface morphology of textured steel (Fig. 5b) exhibits a radically different scenario with respect to the untextured one. Moving from dimple edge to bulk steel for about 5 μm in radial coordinates, it appears a dense distribution of small grains with irregular boundaries, whose areas range from 0.01–0.5 μm^2; while moving further towards bulk steel, it appears a grain pattern similar to the previously observed for the untextured case (Fig. 5a): larger domains (areas: 5–10 μm^2) with polygonal boundaries and "dark" inclusions are recognizable.

Therefore, a grain size reduction is observed in correspondence of laser-affected zone, suggesting the occurrence of phase transition phenomena induced by laser heating. This observation is in agreement with previously reported results [13]. The modified material layer was observed in a few microns spacing: this further observation leads to quantify the radial width of the heat affected zone (HAZ) in agreement with the 2D calculations

recently published by Valette et al. [25]. The radial spread of thermal effects strongly depends on the laser pulse duration, and it is confined in the range of 5–10 μm whenever the interaction time lasts few tens of nanoseconds (such in the present case).

3.2.1. A new model for grain size distribution

This section is dedicated to the new theoretical model developed to interpret the grain size behaviour observed in laser-affected zones.

The energy W of the laser is dissipated in a fraction φ_h for producing the hole, in a fraction φ_m for modifying the material structure around the hole, and in a fraction $1-\varphi_h-\varphi_m$ in other processes. Indicating with Φ the energy spent per unit volume for creating the hole (a "material constant") and with W_h the actual energy spent for creating the hole, we have: $W_h=\varphi_h W=\Phi V_h$, where $V_h=\pi R^2 H f$ is the volume of the hole having radius R and height H (Fig. 6). f is a shape function that equals 1 for the cylindrical shape (Fig. 6a), whereas $f(R,H)=(H/R-(H^2/3R^2))$ for different spherical shapes (Fig. 6b). Note that R for a spherical hole is here defined as the radius of the osculating sphere, and not as the radius of the base of the related spherical cap. Accordingly, the lateral surface of the hole is $S_h=2\pi RH$, independently from its shape. Indicating with γ the total surface energy per unit area required to produce new grain boundaries, we have $W_m=\varphi_m W=\gamma S$, where W_m is the total energy required to produce new grain boundaries and S is the total surface of the grains. Locally, the energy balance becomes: $-\mathrm{d}W_m(x)/\mathrm{d}x=\gamma \mathrm{d}S(x)/\mathrm{d}x$, where x is the radial coordinate which has the origin at the hole surface. The energy penetration into the material is dictated by its absorption coefficient k, according to $W_m(x)=W_m e^{-kx}$, where x is the penetration coordinate. Moreover, the number of grains in the region comprised between x and $x+\mathrm{d}x$ is $\mathrm{d}N=2\pi(R+x)(H+\delta x)\mathrm{d}x/d^3$, where $\delta=0$ for cylindrical holes or $\delta=1$ for spherical holes and d is the grain size. The surface of each grain is $s=\alpha d^2$, where α is a shape constant (e.g. for cubic grains $\alpha=6$). Thus, the total surface is $\mathrm{d}S=s\mathrm{d}N=2\pi(R+x)(H+\delta x)\alpha\,\mathrm{d}x/d$. Accordingly, from the previous local energy balance, the grain size variation is derived in the following form:

$$d(x,R,H)=\frac{2\pi\gamma\alpha(R+x)(H+\delta x)}{W_m k e^{-kx}}=\frac{2\gamma\alpha\varphi_h}{\Phi\varphi_m kR}\frac{(1+x/R)(1+\delta x/H)}{f(R,H)}e^{kx} \quad (1)$$

Note that, mathematically, $d(\infty,R,H)=\infty$ since no energy is available for grain boundary formation at infinity and

$$d(0,R,H)=\frac{2\gamma\alpha\varphi_h}{\Phi\varphi_m kR}\frac{1}{f(R,H)} \quad (2)$$

that is thus predicted to scale inversely to the hole size. Similarly $d(x,0,H)=\infty$ since a vanishing hole size implies a vanishing laser energy, whereas $d(x,\infty,H)=0$, that is, infinitely small grains can be developed using infinite energy.

Note that the hole size is related to the laser energy by

$$R=\sqrt{\frac{\varphi_h W}{\pi\Phi H}\frac{1}{f(R,H)}} \quad (3)$$

e.g., for self-similar holes ($R\propto H$) $R\propto W^{1/3}$.

Further considerations need to be stated in order to identify the limits of validity for this theoretical approach. The model is based on the energy balance that governs the laser-matter interaction, but it does not invoke a time-dependence relationship, neither it explains the direct role of temperature. Thus, the proposed approach cannot predict the nature of the sub-surface phase transitions occurring as "additional effects" due to LST. It is difficult to clarify this point, anyway it can be useful to recall some well known conclusions from metallurgical studies [26–28]. In the ns-pulse duration regime metal melting, matter re-deposition and re-crystallization processes occur as already mentioned in literature [26,27]. Conversely in the femtosecond case, the ultrashort duration of the pulses leads to largely reduced laser-matter interactions, and forces other types of phase transition phenomena such as sublimation. In this regime, which is well suited for micromachining at the sub-micron scale [28], thermal damage is minimal and the HAZ becomes not trivial to recognize with FIB/SEM approach. It is thus necessary to adopt a scanning transmission electron microscopy (STEM) to highlight lattice damage due to mechanical stresses [15]. Therefore, it can be argued that the phenomenology related to the fs-regime is beyond the limits of the proposed model.

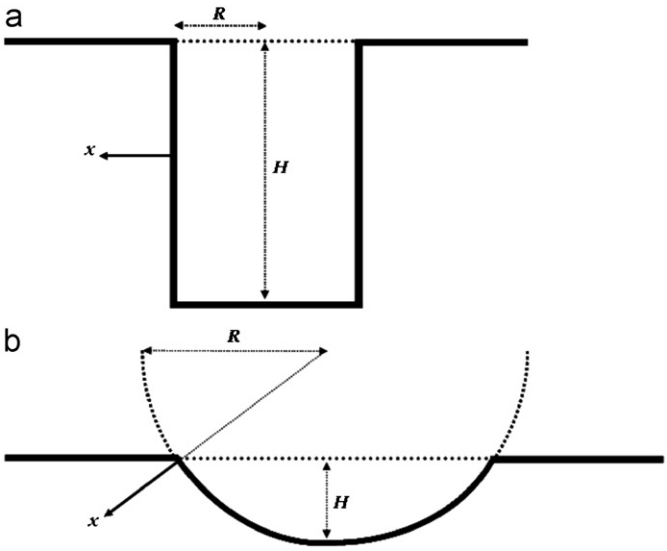

Fig. 6. Simplified sketches which summarize the two geometries, involved in the theoretical model: (a) cylindrical, and (b) spherical. Both approaches imply radial coordinates (x) originating from the surface of the dimple, whose height (H) is defined as maximum depth. Note that for spherical dimples, radius (R) is defined as the radius of the osculating sphere, and is not that of the base of the related cap, such in the cylindrical case.

3.2.2. Numerical fit

In the present case (Fig. 1b), dimple shapes could be approximated as hemi-spherical ($R=H=50\,\mu\mathrm{m}$), because the radius of the osculating sphere coincides with the radius of the hole. Thus, Eq. (1) can be used to fit experimental data in a simplified form, making opportune substitutions ($f=2/3$; $\delta=1$):

$$d(x)=d_0\left(1+\frac{x}{R}\right)^2 e^{kx} \quad (4)$$

where coefficients k and $d_0=3\gamma\alpha\varphi_h/(\Phi\varphi_m kR)$ will be gained as best fit parameters.

Grain analysis was carried out on several FIB images of different discovered walls trenched beside dimples (see an example in Fig. 5b), in order to obtain a statistic collection: up to 80 grains were characterized. Note that model is based on the assumption of constant laser energy (W), and does not take into account other phenomena such as FIB-induced re-annealing during Pt-shield deposition. Grain analysis results are shown in Fig. 7, where best fit function is overlapped to experimental data. Average sizes (d), calculated as square root of grain areas, were plotted against radial distances (x) of the centre of each grain from dimple edge. The distribution is fitted by Eq. (4), obtaining $d_0=(0.24\pm0.03)\,\mu\mathrm{m}$ and $k=(0.23\pm0.02)\,\mu\mathrm{m}^{-1}$ as best fit parameters.

3.3. Sub-surface mechanical characterization and Hall–Petch approach

The experimental analysis on "macro-cross-sectioned" textured steel consists on several matrices of indentations performed on a $20 \times 20\,\mu m^2$ selected area around an individual dimple edge. The distance between two contiguous indentations is about 1 μm (this distance could slightly change in proximity of the border, in order to faithfully follow the shape of the dimple edge).

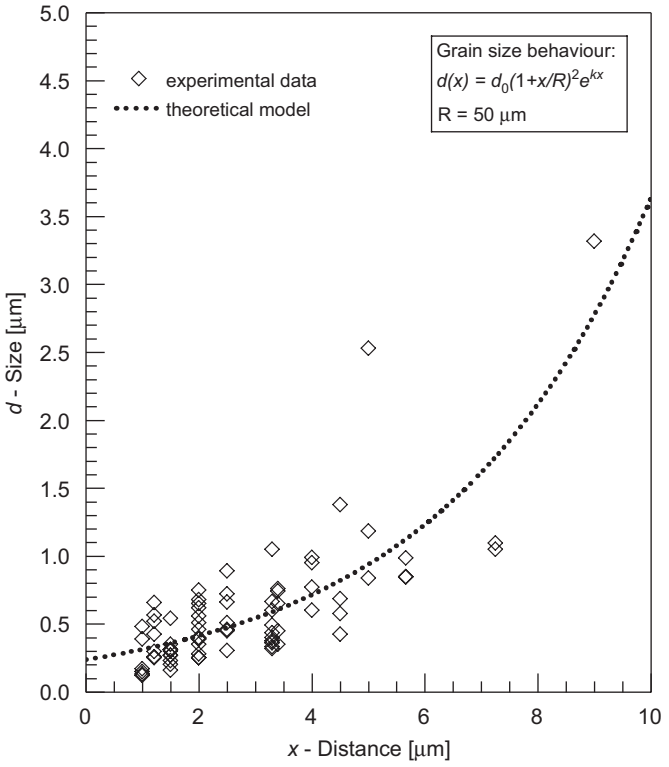

Fig. 7. Diamonds: lateral grain sizes (d) plotted against radial distances (x). Dotted line: best fit of the experimental data by Eq. (4); $d_0 = (0.24 \pm 0.03)\,\mu m$ and $k = (0.23 \pm 0.02)\,\mu m^{-1}$ are the best fit parameters.

In Fig. 8 average values of hardness (H) are plotted against radial distances (x) from dimple edge (error bars are standard deviations). Hardness profile replies the sub-surface morpho-structural trend of laser-affected zones previously described (Section 3.2): hardening occurs as a further consequence of laser-matter interaction, locally confined in HAZ. Moving towards dimple edge nanohardness values increase by a factor of 2, moving from 3500–4000 MPa (for a distance of about 20 μm from dimple edge) up to 7000–7500 MPa (for a distance of about 2 μm from dimple edge).

The final discussion covers the relationship between grain size reduction and hardness increment accordingly to the Hall–Petch behaviour [29,30]:

$$\mathrm{H}(x, R, H) = \mathrm{H}_\infty + hd(x, R, H)^{-1/2} \tag{5}$$

where h is a constant and $\mathrm{H}_\infty = \mathrm{H}(x = \infty)$ represents the hardness of the untextured material. Note that in terms of energy and for self-similar holes, a hardness scaling near the hole has to be taken into consideration: $\mathrm{H}(x = 0, W) = \mathrm{H}_\infty + \bar{h}W^{-1/6}$ (with $\bar{h}$ constant). Introducing Eqs. (1) and (2) into Eq. (5) yields

$$\mathrm{H}(x, R, H) = \mathrm{H}_\infty + hd(0, R, H)^{-1/2} \frac{e^{-kx/2}}{\sqrt{(1 + x/R)(1 + \delta x/H)}} \tag{6}$$

Eq. (6) could be reduced to two simpler forms, which are useful to fit the experimental data. Reminding the hemi-spherical approximation ($R = H = 50\,\mu m$; $f = 2/3$; $\delta = 1$), and introducing Eq. (4), k, and d_0 best fit parameters previously gained (see section 3.2.2) into Eq. (5), yields

$$\mathrm{H}(x) = \mathrm{H}_\infty + hd_0^{-1/2}\left(1 + \frac{x}{R}\right)^{-1} e^{-kx/2} \tag{7}$$

or, introducing an exponential term (β) that will be gained as an additional best fit parameter and is expected to be close to 0.5:

$$\mathrm{H}(x) = \mathrm{H}_\infty + hd_0^{-\beta}\left(1 + \frac{x}{R}\right)^{-2\beta} e^{-k\beta x} \tag{8}$$

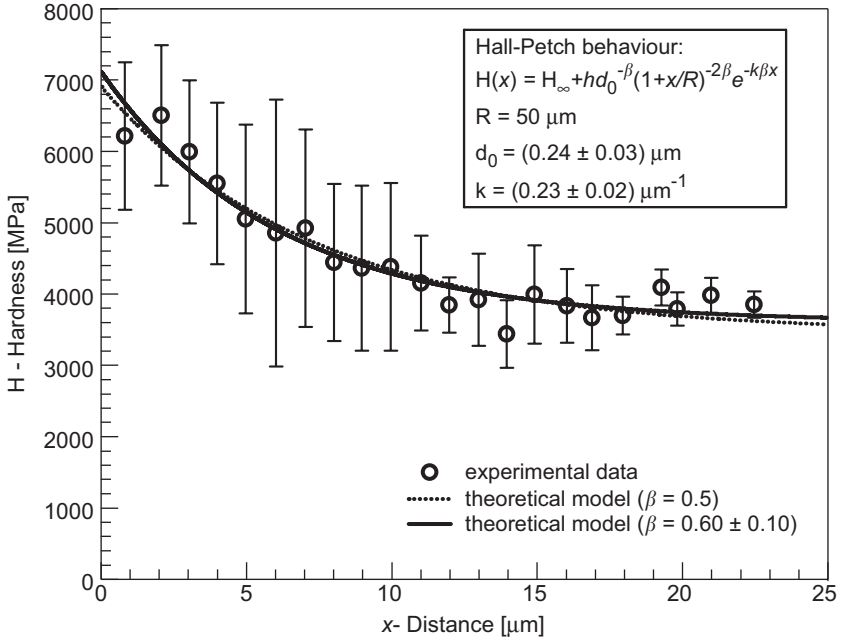

Fig. 8. Circles: local hardness (H) plotted against radial distances (x). Dotted line: best fit of the experimental data by Eq. (7); $h^* = (1690 \pm 110)\,\mathrm{MPa}\,\mu m^{0.5}$ and $\mathrm{H}^*_\infty = (3450 \pm 80)\,\mathrm{MPa}$ are best fit parameters. Continuous line: best fit of the experimental data by Eq. (8); $h^{**} = (1450 \pm 200)\,\mathrm{MPa}\,\mu m^{0.6}$, $\mathrm{H}^{**}_\infty = (3600 \pm 150)\,\mathrm{MPa}$ (coherent with H^*_∞ value), and $\beta = 0.6 \pm 0.1$ (coherent with 0.5 exponent) are the best fit parameters.

where parameters H_{∞} and h will be gained as best fit parameters. Therefore, the experimental data were fitted by using each of the two last custom equations. Note that Eq. (7) faithfully obeys to the Hall–Petch's law, while Eq. (8) includes the term β which identifies the agreement between the system behaviour and the Hall–Petch's law.

Results are shown in Fig. 8, where the numerical fits are overlapped to experimental data distribution. Fitting the data by Eq. (7), we obtained $h^{*} = (1690 \pm 110)\,\mathrm{MPa}\,\mu\mathrm{m}^{0.5}$ and $H^{*}_{\infty} = (3450 \pm 80)\,\mathrm{MPa}$ (dotted line), while fitting the same by Eq. (8) we obtained $h^{**} = (1450 \pm 200)\,\mathrm{MPa}\,\mu\mathrm{m}^{0.6}$, $H^{**}_{\infty} = (3600 \pm 150)$ MPa (coherent with H^{*}_{∞} value), and $\beta = 0.06 \pm 0.1$ coherent with the 0.5 exponent of the Hall–Petch's law (continuous line).

Summarizing, the two best fit functions are very similar and in good agreement with hardness experimental distribution, thus we can conclude that our experimental data are consistent with the Hall–Petch's law.

4. Conclusions

An experimental work was carried out on 30NiCrMo12 nitride steel microdimpled by a Nd:YAG ns-pulse duration laser beam. Tribological tests performed in "full lubrication" configuration showed an improvement of friction behaviour ascribed to the well known hydrodynamic lift effect ensured by microdimples. Average friction coefficients were observed to be reduced by a factor of 2 comparing untextured and textured surfaces.

"Additional effects" due to LST were also discovered and explained. Laser ablation in creating dimples is accompanied to local heating which promotes the formation of a modified material layer confined in HAZ. Thus, morphological, structural and mechanical changes occur in micrometric sub-surface areas near the dimple edges, where two experimental campaigns performed by using FIB and AFM revealed dramatic correlated consequences: grain size reduction and local hardening.

Grain analysis was performed on FIB images: channelling contrast revealed domains distribution, whose dimensions strongly decreased on textured steel moving from bulk to dimple edges. Experimental data were fitted by a custom equation, resulting from a theoretical model which explains grain size behaviour according to the properties of textured material, to the characteristics of laser beam and to the geometry of ablated dimples.

Indentation grids performed by AFM on "macro-cross-sections" revealed an increment of hardness values, which grew up even by a factor of 2 with respect to hardness values measured on bulk, accordingly to Hall–Petch behaviour.

Thus, the previous model was subsequently integrated with Hall–Petch's law, in order to correlate hardening with grain size reduction due to laser-matter interaction. Experimental data are in good agreement with the proposed theoretical model that can thus be used for controlling local hardening due to LST processes carried out in ns-pulse duration regime.

Acknowledgements

The authors are indebted to I. Etsion for useful discussions, to Dr. G.C. Gazzadi and Dr. C. Menozzi for precious collaborations with dual beam system, and to Surface Technologies Ltd (Israel) for LST manufacturing. This work was supported by Regione Emilia Romagna (LR n.7/2002, PRRIITT misura 3.1A). The activity has been performed at the Net-Lab SUP&RMAN.

References

[1] Erdemir A. Review of engineered tribological interfaces for improved boundary lubrication. Tribol Int 2005;38(3):249.
[2] Kovalchenko A, Ajayi O, Erdemir A, Fenske G, Etsion I. The effect of laser surface texturing on transitions in lubrication regimes during unidirectional sliding contact. Tribol Int 2005;38(3):219.
[3] Ryk G, Kligerman Y, Etsion I. Experimental investigation of laser surface texturing for reciprocating automotive components. Tribol Trans 2002;45(4):444.
[4] Ronen A, Etsion I, Kligerman Y. Friction-reducing surface-texturing in reciprocating automotive components. Tribol Trans 2001;44(3):359.
[5] Parry AO, Swain PS, Fox J. Fluid adsorption at a non-planar-wall: roughness-induced first order wetting. Am J Phys Condens Matter 1996;8:L659.
[6] Chow TS. Wetting of rough surfaces. J Phys Condens Matter 1998;10:L445.
[7] Andersson P, Koshinen J, Varjus S, Gerbig Y, Haefke H, Georgiou S, et al. Microlubrication effect by laser-textured steel surfaces. Wear 2007;262:369.
[8] Haefke H, Gerbig Y, Dimitru G, Romano V. Microtexturing of functional surfaces for improving their tribological performance. In: Proceedings of the international tribology conference, Nagasaki, 2000. p. 217.
[9] Etsion I. State of the art in laser surface texturing. J Tribol 2005;127:248.
[10] Hoppermann A, Kordt M. Tribological optimization using laser-structured contact surfaces. Ölhydraulik und Pneumatik 2002:46.
[11] Dumitru G, Romano V, Weber HP, Haefke H, Gerbig Y, Pflüger E. Laser microstructuring of steel surfaces for tribological applications. Appl Phys A 2000;70:485.
[12] Borghi A, Gualtieri E, Marchetto D, Moretti L, Valeri S. Tribological effects of surface texturing on nitriding steel for high-performance engine applications. Wear 2008;265:1046.
[13] Obergfell K, Schulze V, Vohringer O. Classification of microstructural changes in laser hardened steel surfaces. Mat Sci Eng A 2003;355:348.
[14] Bello JM, Fernandez BJ, Lopez V, Ruiz J. Fatigue performance and residual stresses in laser treated 50CrV4 steel. J Mater Sci 1994;29:5213.
[15] Coyne E, Magee JP, Mannion P, O'Connor GM, Glynn TJ. STEM analysis of femtosecond laser pulse induced damage to bulk silicon. Appl Phys A Mat Sci Proc 2005;81:371.
[16] Shakvorostov D, Pohlmann K, Scherge M. Structure and mechanical properties of tribologically induced nanolayers. Wear 2006;260:433.
[17] Xie Z-H, Munroe PR, Moon RJ, Hoffmann M. Characterization of surface contact-induced fracture in ceramics using a focused ion beam miller. Wear 2003;255:651.
[18] Bolelli G, Cannillo V, Lusvarghi L, Pighetti Mantini F, Gualtieri E, Menozzi C. A FIB study of sharp indentation testing on plasma-sprayed TiO_2. Mater Lett 2008;62:1557.
[19] Bhushan B, Koinkar VN. Nanoindentation hardness measurements using atomic force microscopy. Appl Phys Lett 1994;64(13):1653.
[20] Calabri L, Pugno N, Rota A, Marchetto D, Valeri S. Nanoindentation shape-effect: experiments, simulations and modelling. J Phys Condens Matter 2007;19:395002.
[21] Orloff J, Utlaut M, Swanson L. High resolution focused ion beams: FIB and its applications. New York: Kluwer Academic/Plenum Press; 2003. p. 130–33, 245–50.
[22] Pharr GM, Oliver WC, Brotzen FR. On the generality of the relationship among contact stiffness, contact area, and elastic modulus during indentation. J Mat Res 1992;7(6):613.
[23] Oliver WC, Pharr GM. An improved technique for determining hardness and elastic modulus using load and displacement sensing indentation experiments. J Mat Res 1992;7(6):1564.
[24] Oliver WC, Pharr GM. Measurement of hardness and elastic modulus by instrumented indentation: advances in understanding and refinements to methodology. J Mat Res 2004;19:1.
[25] Valette S, Le Harzic R, Huot N, Audouard E, Fortunier R. 2D calculations of the thermal effects due to femtosecond laser–metal interaction. Appl Surf Sci 2005;247:238.
[26] Zhu X, Naumov AY, Villeneuve DM, Corkum PB. Influence of laser parameters and material properties on micro drilling with femtosecond laser pulses. Appl Phys A Mat Sci Proc 1999;69:S367.
[27] Chichkov BN, Momma C, Nolte S, von Alvensleben F, Tünnermann A. Femtosecond, picosecond and nanosecond laser ablation of solid. Appl Phys A Mat Sci Proc 1996;63(2):109.
[28] Mourier L, Mazuyer D, Lubrecht AA, Donnet C, Audouard E. Action of a femtosecond laser generated micro-cavity trough a circular EHL contact. Wear 2008;264:450.
[29] Hall EO. The deformation and ageing of mild steel: III discussion of results. Proc Phys Soc B 1951;64:747.
[30] Petch NJ. The cleavage strength of polycrystals. J Iron Steel Inst 1953:25.